



Resolving adjacent nanophosphors of different concentrations by excitation-based cone-beam X-ray luminescence tomography

PENG GAO,^{1,2} HUANGSHENG PU,^{1,2} JUNYAN RONG,¹ WENLI ZHANG,¹
TIANSHUAI LIU,¹ WENLEI LIU,¹ YUANKE ZHANG,¹ AND HONGBING LU^{1,*}

¹Department of Biomedical Engineering, Fourth Military Medical University, Xi'an, Shaanxi 710032, China

²These authors contributed equally to this work

*luhb@fmmu.edu.cn

Abstract: Cone-beam X-ray luminescence computed tomography (CB-XLCT) has been proposed as a new molecular imaging modality recently. It can obtain both anatomical and functional tomographic images of an object efficiently, with the excitation of nanophosphors *in vivo* or *in vitro* by cone-beam X-rays. However, the ill-posedness of the CB-XLCT inverse problem degrades the image quality and makes it difficult to resolve adjacent luminescent targets with different concentrations, which is essential in the monitoring of nanoparticle metabolism and drug delivery. To address this problem, a multi-voltage excitation imaging scheme combined with principal component analysis is proposed in this study. Imaging experiments performed on physical phantoms by a custom-made CB-XLCT system demonstrate that two adjacent targets, with different concentrations and an edge-to-edge distance of 0 mm, can be effectively resolved.

© 2017 Optical Society of America

OCIS codes: (100.3010) Image reconstruction techniques; (110.6960) Tomography; (100.3190) Inverse problems; (170.3880) Medical and biological imaging; (110.7440) X-ray imaging; (170.3660) Light propagation in tissues.

References and links

1. C. M. Carpenter, C. Sun, G. Pratz, R. Rao, and L. Xing, "Hybrid x-ray/optical luminescence imaging: Characterization of experimental conditions," *Med. Phys.* **37**(8), 4011–4018 (2010).
2. G. Pratz, C. M. Carpenter, C. Sun, R. P. Rao, and L. Xing, "Tomographic molecular imaging of x-ray-excitable nanoparticles," *Opt. Lett.* **35**(20), 3345–3347 (2010).
3. G. Pratz, C. M. Carpenter, C. Sun, and L. Xing, "X-ray luminescence computed tomography via selective excitation: a feasibility study," *IEEE Trans. Med. Imaging* **29**(12), 1992–1999 (2010).
4. M. Ahmad, G. Pratz, M. Bazalova, and L. Xing, "X-ray luminescence and x-ray fluorescence computed tomography: new molecular imaging modalities," *IEEE Access* **2**, 1051–1061 (2014).
5. W. Cong, G. Wang, D. Kumar, Y. Liu, M. Jiang, L. Wang, E. Hoffman, G. McLennan, P. McCray, J. Zabner, and A. Cong, "Practical reconstruction method for bioluminescence tomography," *Opt. Express* **13**(18), 6756–6771 (2005).
6. G. Wang, W. Cong, K. Durairaj, X. Qian, H. Shen, P. Sinn, E. Hoffman, G. McLennan, and M. Henry, "In vivo mouse studies with bioluminescence tomography," *Opt. Express* **14**(17), 7801–7809 (2006).
7. J. Feng, K. Jia, G. Yan, S. Zhu, C. Qin, Y. Lv, and J. Tian, "An optimal permissible source region strategy for multispectral bioluminescence tomography," *Opt. Express* **16**(20), 15640–15654 (2008).
8. R. B. Schulz, A. Ale, A. Sarantopoulos, M. Freyer, E. Soehngen, M. Zientkowska, and V. Ntziachristos, "Hybrid system for simultaneous fluorescence and x-ray computed tomography," *IEEE Trans. Med. Imaging* **29**(2), 465–473 (2010).
9. H. Pu, W. He, G. Zhang, B. Zhang, F. Liu, Y. Zhang, J. Luo, and J. Bai, "Separating structures of different fluorophore concentrations by principal component analysis on multispectral excitation-resolved fluorescence tomography images," *Biomed. Opt. Express* **4**(10), 1829–1845 (2013).
10. A. Soubret and V. Ntziachristos, "Fluorescence molecular tomography in the presence of background fluorescence," *Phys. Med. Biol.* **51**(16), 3983–4001 (2006).
11. C. Li, A. M. Dávalos, and S. R. Cherry, "Numerical and experimental studies of x-ray luminescence optical tomography for small animal imaging," in *SPIE BiOS*, (International Society for Optics and Photonics, 2013), pp. 85781B.
12. C. Li, A. Martínez-Dávalos, and S. R. Cherry, "Numerical simulation of x-ray luminescence optical tomography for small-animal imaging," *J. Biomed. Opt.* **19**(4), 046002 (2014).

13. W. Cong and G. Wang, "X-ray fan-beam luminescence tomography," *Austin J. Biomed. Eng.* **1**(5), 1024 (2014).
14. D. Chen, S. Zhu, H. Yi, X. Zhang, D. Chen, J. Liang, and J. Tian, "Cone beam x-ray luminescence computed tomography: A feasibility study," *Med. Phys.* **40**(3), 031111 (2013).
15. X. Liu, Q. Liao, and H. Wang, "In vivo x-ray luminescence tomographic imaging with single-view data," *Opt. Lett.* **38**(22), 4530–4533 (2013).
16. X. Liu, Q. Liao, and H. Wang, "Fast X-ray luminescence computed tomography imaging," *IEEE Trans. Biomed. Eng.* **61**(6), 1621–1627 (2014).
17. X. Liu, H. Wang, M. Xu, S. Nie, and H. Lu, "A wavelet-based single-view reconstruction approach for cone beam x-ray luminescence tomography imaging," *Biomed. Opt. Express* **5**(11), 3848–3858 (2014).
18. G. Zhang, F. Liu, J. Liu, J. Luo, Y. Xie, J. Bai, and L. Xing, "Cone Beam X-ray Luminescence Computed Tomography Based on Bayesian Method," *IEEE Trans. Med. Imaging* **36**(1), 225–235 (2017).
19. Z. Liu, Z. Li, J. Liu, S. Gu, Q. Yuan, J. Ren, and X. Qu, "Long-circulating Er^{3+} -doped Yb_2O_3 up-conversion nanoparticle as an in vivo X-Ray CT imaging contrast agent," *Biomaterials* **33**(28), 6748–6757 (2012).
20. Z. Liu, F. Pu, S. Huang, Q. Yuan, J. Ren, and X. Qu, "Long-circulating $\text{Gd}_2\text{O}_3\text{:Yb}^{3+}$, Er^{3+} up-conversion nanoprobe as high-performance contrast agents for multi-modality imaging," *Biomaterials* **34**(6), 1712–1721 (2013).
21. L. Xiong, T. Yang, Y. Yang, C. Xu, and F. Li, "Long-term in vivo biodistribution imaging and toxicity of polyacrylic acid-coated upconversion nanophosphors," *Biomaterials* **31**(27), 7078–7085 (2010).
22. Z. Yi, W. Lu, Y. Xu, J. Yang, L. Deng, C. Qian, T. Zeng, H. Wang, L. Rao, H. Liu, and S. Zeng, "PEGylated $\text{NaLuF}_4\text{:Yb/Er}$ upconversion nanophosphors for in vivo synergistic fluorescence/X-ray bioimaging and long-lasting, real-time tracking," *Biomaterials* **35**(36), 9689–9697 (2014).
23. X. Liu, Q. Liao, H. Wang, and Z. Yan, "Excitation-resolved cone-beam x-ray luminescence tomography," *J. Biomed. Opt.* **20**(7), 070501 (2015).
24. H. Abdi and L. J. Williams, "Principal component analysis," *Wiley Interdiscip. Rev. Comput. Stat.* **2**(4), 433–459 (2010).
25. L. V. Wang and H.-i. Wu, *Biomedical optics: principles and imaging* (John Wiley & Sons, 2012).
26. A. D. Klose, V. Ntziachristos, and A. H. Hielscher, "The inverse source problem based on the radiative transfer equation in optical molecular imaging," *J. Comput. Phys.* **202**(1), 323–345 (2005).
27. A. Kak and M. Slaney, *Computerized Tomographic Imaging* (New York: IEEE Press, 1987), chap. 7.
28. I. Kandarakis, D. Cavouras, G. Panayiotakis, T. Agelis, C. Nomicos, and G. Giakoumakis, "X-ray induced luminescence and spatial resolution of $\text{La}_2\text{O}_2\text{S:Tb}$ phosphor screens," *Phys. Med. Biol.* **41**(2), 297–307 (1996).
29. X. Liu, D. Wang, F. Liu, and J. Bai, "Principal component analysis of dynamic fluorescence diffuse optical tomography images," *Opt. Express* **18**(6), 6300–6314 (2010).
30. H. Pu, G. Zhang, W. He, F. Liu, H. Guang, Y. Zhang, J. Bai, and J. Luo, "Resolving fluorophores by unmixing multispectral fluorescence tomography with independent component analysis," *Phys. Med. Biol.* **59**(17), 5025–5042 (2014).
31. L. Feldkamp, L. Davis, and J. Kress, "Practical cone-beam algorithm," *J. Opt. Soc. Am. A* **1**(6), 612–619 (1984).
32. Y. Zhou, H. Guang, H. Pu, J. Zhang, and J. Luo, "Unmixing multiple adjacent fluorescent targets with multispectral excited fluorescence molecular tomography," *Appl. Opt.* **55**(18), 4843–4849 (2016).
33. H. Yi, D. Chen, W. Li, S. Zhu, X. Wang, J. Liang, and J. Tian, "Reconstruction algorithms based on L1 -norm and L2 -norm for two imaging models of fluorescence molecular tomography: a comparative study," *J. Biomed. Opt.* **18**(5), 056013 (2013).
34. L. Sudheendra, G. K. Das, C. Li, D. Stark, J. Cena, S. Cherry, and I. M. Kennedy, " $\text{NaGdF}_4\text{:Eu}^{3+}$ nanoparticles for enhanced x-ray excited optical imaging," *Chem. Mater.* **26**(5), 1881–1888 (2014).

1. Introduction

X-ray luminescence computed tomography (XLCT) has been proposed as a promising hybrid molecular imaging modality in recent years with the development of X-ray excitable rare earth nanophosphors [1–4]. When irradiated by X-rays, nanophosphors in the imaging object emit visible or near-infrared (NIR) light that can be detected by an optical detector. Based on the imaging and reconstruction model, the distribution and concentration of the nanophosphors inside imaging object can be resolved. Compared with other optical molecular imaging such as bioluminescence tomography (BLT) [5–7] and fluorescence molecular tomography (FMT) [8–10], XLCT has several advantages with the use of X-rays. Firstly, X-ray can penetrate the imaging object easily and provide more information deep inside the object. Secondly, the optical background can be avoided since X-ray is used as the excitation source to eliminate the autofluorescence, which helps to further improve the spatial resolution of optical imaging. As a hybrid X-ray/optical imaging modality, XLCT can

obtain anatomical and functional information simultaneously and is becoming a potential imaging technique for fundamental research and preclinical experiments.

Continuous efforts have been made in XLCT imaging since it was first demonstrated by Xing's group [2]. The narrow-beam and pencil-beam XLCT showed good spatial resolution and imaging depth at the cost of long imaging time [3, 11, 12]. For fast imaging, fan-beam [13] and cone beam XLCT (CB-XLCT) imaging systems were investigated. Though the fan-beam mode can achieve fast data acquisition than narrow-beam and pencil-beam XLCT and reliable image reconstruction than CB-XLCT, it is not suitable for whole body imaging *in vivo* for the time-consuming slice-by-slice scanning mode. Computer simulations and experiments with phantoms demonstrate that CB-XLCT is more efficient and suitable for *in vivo* research [14–18]. In *in vivo* studies, some rare earth nanophosphors showed a long blood circulation time [19–22], and in some cases the retention took place primarily in the reticuloendothelial system (RES) such as liver and spleen [19, 21]. During a short period, the nanophosphors concentrations in liver and spleen can be seen as different but constant. As a result, the capability of CB-XLCT to differentiate adjacent nanophosphors with different concentrations would be essential. However, due to high scattering properties of light in biological tissues, the reconstruction of CB-XLCT is an ill-posed and ill-conditioned problem. Though some effort has been devoted to the differentiation of adjacent luminescence targets filled with different nanophosphors [23], no studies have been reported to resolve adjacent luminescent targets with different concentrations so far.

Our phantom experiments indicate that nanophosphors of different concentrations behave differently when excited by X-rays of different energies. In this study, to resolve adjacent targets with different concentrations, a multi-voltage excitation scheme is first proposed. Then the principal component analysis (PCA) [24] is applied to multi-voltage XLCT reconstructions to separate targets with different behaviors. Imaging experiments with physical phantoms demonstrate the feasibility of the proposed method on resolving two adjacent targets with different concentrations.

The paper is organized as follows. In Section 2, the basic theories of the proposed algorithm and the phantom experiments setups are detailed. In Section 3, the results are described. Finally, the major findings of this study are discussed and concluded in Section 4.

2. Methods

2.1 Forward and inverse problems

X-rays emitted from the X-ray source travel through tissues or a phantom, and irradiate nanophosphors inside to emit visible or near-infrared light (NIR). The light intensity can be expressed as follows [14–17]:

$$S(\mathbf{r}) = \varepsilon X(\mathbf{r}) \rho(\mathbf{r}) \quad (1)$$

where ε is the light yield of the nanophosphors, and $X(\mathbf{r})$ and $\rho(\mathbf{r})$ represent the X-ray intensity and nanophosphor concentration at position \mathbf{r} , respectively. According to Lambert-Beers' law, $X(\mathbf{r})$ can be expressed as:

$$X(\mathbf{r}) = X(\mathbf{r}_0) \exp\left\{-\int_{r_0}^r \mu_t(\tau) d\tau\right\} \quad (2)$$

where $X(\mathbf{r}_0)$ is the X-ray source intensity at the initial position \mathbf{r}_0 , and $\mu_t(\tau)$ is the X-ray attenuation coefficient of tissues at position τ , which can be obtained from the CT images.

Due to the high scattering properties of light in biological tissues, the visible or NIR light transported in these tissues can be expressed by the diffusion equation (DE) [25]:

$$-\nabla[D(\mathbf{r})\nabla\Phi(\mathbf{r})] + \mu_a(\mathbf{r})\Phi(\mathbf{r}) = S(\mathbf{r}) \quad (\mathbf{r} \in \Omega) \quad (3)$$

where Ω is the domain of the imaged object, $\Phi(\mathbf{r})$ is the photon fluence at position \mathbf{r} , $D(\mathbf{r})$ is the diffusion coefficient and can be calculated by $D(\mathbf{r}) = (3(\mu_a(\mathbf{r}) + \mu'_s(\mathbf{r})))^{-1}$, where $\mu_a(\mathbf{r})$ and $\mu'_s(\mathbf{r})$ are the absorption and reduced scattering coefficient of the tissue, respectively. The DE can be further complemented by the Robin boundary condition [26]:

$$\Phi(\mathbf{r}) + 2\alpha D(\mathbf{r})[\mathbf{v}\nabla\Phi(\mathbf{r})] = 0 \quad (\mathbf{r} \in \partial\Omega) \quad (4)$$

where $\partial\Omega$ is the boundary of Ω , \mathbf{v} is the outward unit normal vector on $\partial\Omega$, and α is the boundary mismatch factor, depending on the optical reflective index mismatch at the boundary.

By using the finite-element method (FEM), Eq. (2) and Eq. (3) can be discretized into the following matrix equation representing the relationship between the nanophosphor concentration \mathbf{p} and photon measurements on the object surface Φ_{meas} [5]:

$$\mathbf{A}\mathbf{p} = \Phi_{\text{meas}} \quad (5)$$

where \mathbf{A} is a weight matrix used to map the unknown nanophosphor distribution to the known measurements. In this study, for photon measurements acquired at certain X-ray tube voltage, the unknown \mathbf{p} is obtained by solving Eq. (5) using the algebraic reconstruction technique (ART) [27] for its convenience and popularity with the nonnegative constraint.

In previous XLCT studies, the light yield ε is usually considered constant. However, some studies on X-ray excited nanophosphors have indicated that the light yield varies with X-ray tube voltage [28]. That means for a given kind of nanophosphors, ε has its specific variation along the energy spectrum of the excitation X-ray. In this work, we have found that for the same nanophosphor with different concentrations, the changing pattern of ε along the energy spectrum is somehow different, which can be used to separate nanophosphors with different concentrations. That is the foundation of PCA.

2.2 PCA method

PCA is a widely used multivariate analysis technique, which can be used to analyze the structure of the observations. By transforming the original variables to a set of uncorrelated and reordered new variables (PCs) through coordinate system translation, the behaviors of the observations can be resolved [24, 29].

Suppose the reconstructed multi-voltage XLCT images are denoted as $X = \{X_1, X_2, \dots, X_b, \dots, X_N\}$, while N is the number of X-ray tube voltages used in the experiment, and X_i is the reconstructed nanophosphor distribution excited at a given tube voltage, represented as a $M \times I$ column vector consisting of all pixels. In this study, to resolve targets with different concentrations, PCA is applied on the reconstructed XLCT images acquired at different X-ray tube voltages. Then the input data for PCA can be arranged as a $M \times N$ matrix \mathbf{X} and its principal components can be obtained by:

$$\mathbf{P} = \mathbf{X}_0 \times \mathbf{E} \quad (6)$$

where \mathbf{X}_0 is a data set obtained from \mathbf{X} by subtracting its mean value, and \mathbf{E} is the eigenvector matrix. The column of \mathbf{E} is the eigenvector of the following matrix \mathbf{L} :

$$\mathbf{L} = \frac{1}{M-1} \mathbf{X}_0^T \mathbf{X}_0 \quad (7)$$

$$\mathbf{L} = \mathbf{E} \mathbf{\Lambda} \mathbf{E}^T \quad (8)$$

where \mathbf{X}_0^T , \mathbf{E}^T is the transposed matrix of \mathbf{X}_0 , \mathbf{E} , and $\mathbf{\Lambda}$ is a diagonal matrix.

The j -th column of \mathbf{P} is the j -th principal component (PC) of \mathbf{X} , which is a linear combination of \mathbf{X}_0 , and can be expressed as follows,

$$P_j = \mathbf{X}_0 \times E_j \quad (9)$$

where E_j is the j -th column of \mathbf{E} . In this study, by analyzing the distribution of different nanophosphor concentrations in each PC of multi-voltage XLCT images, we propose a PC-based decomposition method to resolve two adjacent targets with different concentrations.

2.3 Setups of phantom experiments

A custom-made CB-XLCT system developed in our laboratory was adopted to conduct the phantom experiments. A schematic diagram of the imaging system is shown in Fig. 1. The XLCT system consists of a micro-focus X-ray source with a tungsten anode (Source-Ray, SB-80-500, N.Y.), a highly sensitive electron-multiplying CCD (EMCCD) camera (iXon DU-897, Andor, U.K.), which is coupled with a 50-mm f/1.8D lens (Nikon, Melville, N.Y.) for optical imaging, and a CMOS X-ray flat-panel detector (2923, Dexela, U.K.) for high resolution CT imaging. The max voltage of the X-ray tube is 80 kV and the max current is 0.5 mA. The CMOS flat-panel detector has an image matrix of 3888×3072 , with a pixel size of $74.8 \mu\text{m}$. The EMCCD camera was positioned perpendicular to the source-detector axis to collect light images of size 512×512 . A lead shield with a hole of diameter 5 cm was positioned in front of the CCD camera to minimize X-ray ionizing radiation.

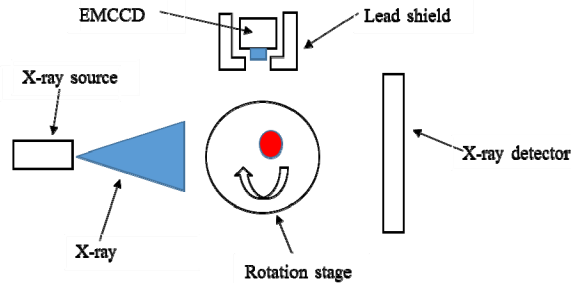


Fig. 1. Schematic diagram of the CB-XLCT system.

The phantom used in this study was a transparent glass cylinder with the outside diameter of 3.0 cm. The cylinder was filled with 1% intralipid solution, with the absorption coefficient $\mu_a = 0.02 \text{ cm}^{-1}$ and reduced scattering coefficient $\mu'_s = 10 \text{ cm}^{-1}$. A widely-used X-ray excited nanophosphor, $\text{Y}_2\text{O}_3:\text{Eu}^{3+}$ (Jiangxi Illuma Fluorescent Materials Co., Ltd., China) was utilized for XLCT imaging. Four small transparent glass tubes with outer diameter of 0.4 cm and inner diameter of 0.3 cm were filled with nanophosphors of concentrations 50, 100, 150, 200 mg/ml, respectively. With the cylinder and four glass tubes, four phantom experiments were performed.

In the first phantom experiment, each of the four glass tubes was positioned at the center of the cylinder and luminescent images excited by X-rays of different energies were obtained at a fixed view. The X-ray tube voltage changed from 40 kV to 80 kV at an increase step of 10 kV, with a constant tube current of 0.5 mA. The experiment was designed to illustrate the light yield of nanophosphors of different concentrations when excited by X-rays at different tube voltages.

To evaluate the influence of tube voltage setting on the differentiation of nanophosphor concentrations, the second phantom experiment was performed using a physical phantom shown in Fig. 2. A pair of tubes containing 50 mg/ml and 100 mg/ml nanophosphors, respectively, was placed seamlessly in the middle of the cylinder, with the edge-to-edge distance (EED) of 0 mm. The nanophosphors in the phantom were irradiated by a series of X-rays with the tube voltages ranging from 40 to 80 kV at an increase step of 10 kV, respectively, under a constant current of 0.5 mA. The exposure time of EMCCD was set to 0.3 s, and the EM gain was set to 260, with 1×1 binning. The luminescence images were

acquired at a 15° step during a 360° span. The X-ray projections were acquired at a 1° step during a 360° span to get the physical structure and corresponding X-ray attenuation map of the phantom.

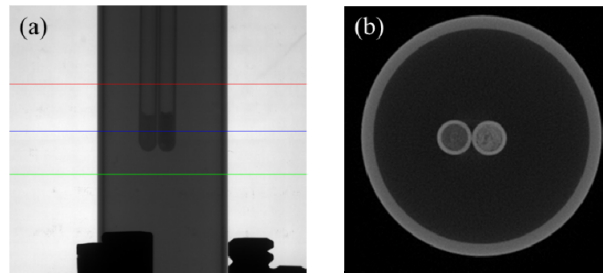


Fig. 2. Illustration of the second phantom experiment. (a) Representative X-ray projection of the phantom. The region between the red and green lines was used for this study. (b) Representative CT image slice of the phantom, corresponding to the slice indicated by the blue line in (a). The nanophosphor concentration of the left tube was 50 mg/ml, and that of the right tube was 100 mg/ml, respectively.

In the third experiment, three pairs of tubes containing nanophosphors of different concentrations, as shown in Table 1, were used to evaluate the influence of concentration difference on the differentiation. Three pairs of tubes were placed in the middle of the cylinder and excited by X-rays with voltage set as 40 kV and 50 kV, respectively, as shown in Fig. 3. For each case, the imaging protocol was the same as that in the second experiment, unless otherwise stated.

In the fourth experiment, two tubes containing nanophosphors of 50 mg/ml and 100 mg/ml were used to evaluate the performance of the proposed method in fan-beam mode and cone-beam mode. In the fan-beam mode experiment, the X-ray beam thickness was collimated to 1 mm. The imaging protocol was the same as that in the third experiment.

Table 1. Tube pairs of different concentrations used in the third experiment

Concentration pairs (mg/ml)	X-ray voltages (kV)
50-50	40,50
50-150	40,50
50-200	40,50

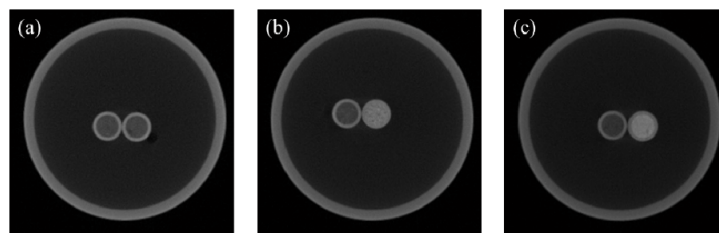


Fig. 3. Illustration of three tube pairs used in the third experiment. Nanophosphor concentrations in (a), (b) and (c) were 50-50, 50-150, 50-200 mg/ml, respectively. The left tube in each image contained nanophosphors of 50 mg/ml.

The total count of photons obtained at a given tube voltage was calculated by summing up all the photons in the luminescent image, followed by the subtraction of background noise, which was obtained without X-ray excitation. For XLCT reconstruction, each phantom was discretized into 2,314 nodes and 10,909 tetrahedral elements in a 3D region of size $3.0 \times 3.0 \times 2.2 \text{ cm}^3$, and the reconstruction was terminated after 300 ART iterations empirically and the relaxation factor was 0.1 [30]. For cone-beam CT reconstruction, the widely-used Feldkamp-Davis-Kress (FDK) method was employed [31].

3. Results

3.1 CCD output of nanophosphors excited by X-rays of different energies

Figure 4 shows the total photon counts detected by CCD when excited under various X-ray tube voltages. It shows that for nanophosphors with different concentrations, the changing rates of photon counts, indicating the light yield trends, varies with the increase of tube voltage. The higher the concentration is, the faster the photon count increases.

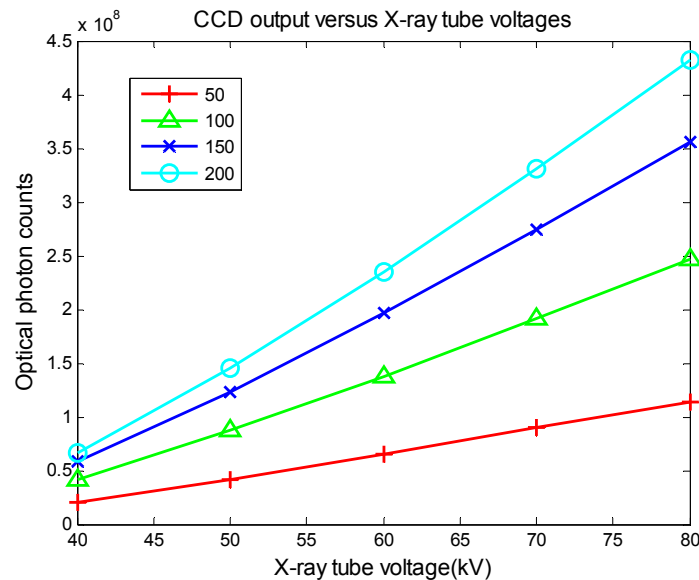


Fig. 4. Optical photon counts excited under different X-ray tube voltages.

3.2 The influence of voltage setting on target differentiation

Figure 5 shows XLCT tomographic images reconstructed from the 50-100 mg/ml concentration pair acquired at different tube voltages ($z = 1.1$ mm, corresponding to the blue line shown in Fig. 2(a)). It indicates that there is no much difference between reconstructed images excited at different voltages. It is difficult to resolve two adjacent luminescence targets from images reconstructed from measurements acquired at a given voltage by the conventional ART algorithm.

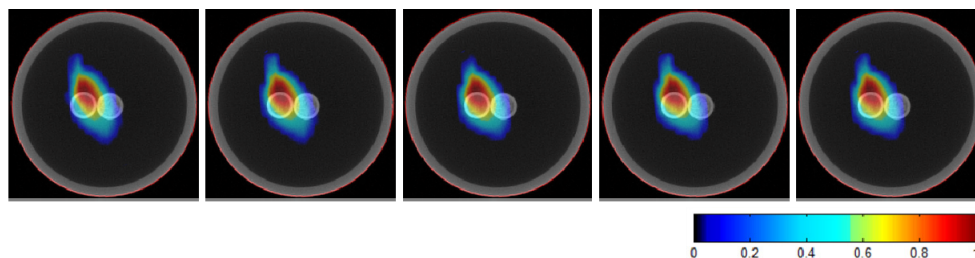


Fig. 5. Tomographic images of the nanophosphor distribution reconstructed from EMCCD measurements acquired at various tube voltages (from left to right, tube voltage is 40, 50, 60, 70, and 80 kV, respectively. $z = 1.1$ mm). The red curve in each image represents the outer boundary of the phantom acquired from white light images. All the XLCT images are displayed in the same range.

Base on the above XLCT images of the 50-100 mg/ml concentration pair acquired at different X-ray tube voltages, PCA was applied on different combinations of XLCT images,

as shown in Table 2. The $N \times N$ eigenvector matrix \mathbf{E} is obtained, and the columns of \mathbf{E} are arranged in the order of decreasing component variance. After analysing the eigenvectors of all the combinations, we find that all the elements in eigenvector E_1 are quite similar which means PC1-XLCT is approximately the mean value of N variables in \mathbf{X}_0 . There are both positive and negative elements in eigenvector E_2 . They are used as weight factors for creating PC2-XLCT images. For example, the obtained eigenvectors in case 4 are listed in Table 3. It demonstrates that the PC2-XLCT is almost the result of variable 2 minus variable 1 in \mathbf{X}_0 , which illustrates that PC2-XLCT is nearly the difference of the two variables in \mathbf{X}_0 .

Table 2. Different combinations of XLCT images acquired at various X-ray voltages

Case #	Number of XLCT images	X-ray voltages (kV)
Case 1	5	40,50,60,70,80
Case 2	4	40,50,60,70
Case 3	3	40,50,60
Case 4	2	40,50

Table 3. The eigenvectors E_1 and E_2 for case 4

E_1	E_2
0.7086	-0.7056
0.7056	0.7086

The second principal component images (PC2-XLCT) generated from different combinations of XLCT images is illustrated in Fig. 6. In cases 1 to 3, the tube containing 50 mg/ml nanophosphors can be reflect by the negative part of the PC2-XLCT, while the tube of 100 mg/ml nanophosphors can be reflected by its positive part. While in case 4, with only two XLCT images acquired at two tube voltages, though the representing of two tubes of different concentrations with negative and positive parts of PC2 is opposite to other cases, the two tubes can still be distinguished by the positive and negative parts. These results demonstrate that when applying PCA on multi-voltage reconstructed XLCT images, the two tubes containing nanophosphors of different concentrations can be differentiated in all cases. To demonstrate the performance of the proposed method more directly, 3D visualizations of the negative and positive parts of PC2 images are shown in Fig. 6.

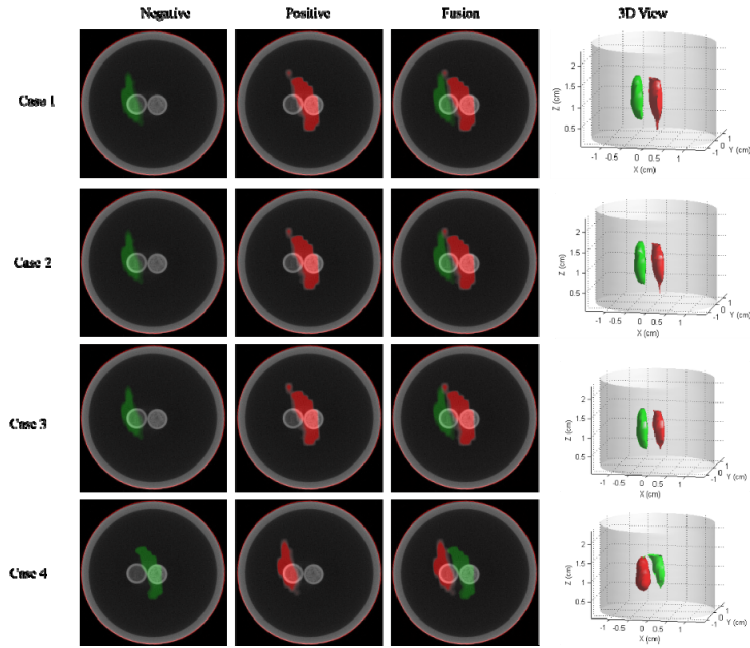


Fig. 6. Tomographic ($z = 1.1$ cm) and 3D results of PC2 obtained from different combinations of XLCT images acquired at various tube voltages. All the images are displayed in the same range. The values below 35% of the maximum are set as zero in the 3D results.

To evaluate the performance of the proposed method on localization accuracy when using different combinations of multi-voltage XLCT images, the distance of centroids (DOC) between the corresponding CT image (as the reference) and PC2-XLCT is used for quantitative evaluation. The centroids of a region of interest can be defined as [32]:

$$\mathbf{u} = \frac{1}{N} \sum_{\mathbf{x} \in Q} \mathbf{x} \quad (10)$$

where \mathbf{u} is the positional vector of the centroid in the Cartesian coordinate system, Q represents all the pixels within the region of interest, N is the number of pixels in Q , and \mathbf{x} stands for the positional vector of a single pixel. The DOC of two tubes can be calculated when its centroid in the CT image \mathbf{u}_{ct} and that in the PC2-XLCT \mathbf{u}_{pc2} are obtained:

$$\text{DOC} = \|\mathbf{u}_{pc2} - \mathbf{u}_{ct}\|_2 \quad (11)$$

where $\|\cdot\|_2$ represents Euclidean metric.

Table 4 shows the DOCs of two tubes for four cases shown in Table 2 in the second phantom experiments. It can be seen that all the DOCs are within 2 mm and are acceptable for localizing the luminescence targets [32] even when the number of exciting tube voltages is reduced to two.

Table 4. DOCs of the proposed method by using different combinations of multi-voltage XLCT images

Case #	DOC (mm)	
	Tube 1	Tube 2
Case 1	1.54	1.32
Case 2	1.58	1.34
Case 3	1.49	1.35
Case 4	1.79	1.22

Considering the ionizing radiation of X-rays, less scans would be of more benefit. Since the two tubes can be separated by the proposed method even using only two XLCT images. To further investigate the effect of their voltage difference on the performance, different combinations of two XLCT images were further tested, as listed in Table 4. The reconstruction results are shown in Fig. 7 and the DOCs are given in Table 5. It indicates that for all the cases using only two XLCT images of different voltages, the two tubes can be separated effectively and the DOCs are acceptable. The location errors are getting smaller as the differences of the two excitation voltages increase.

Table 5. DOCs of the proposed method with different two excitation voltages

Case #	X-ray voltages (kV)	DOC	
		Tube 1 (mm)	Tube 2 (mm)
Case 4	40,50	1.79	1.22
Case 5	40,60	1.49	0.99
Case 6	40,70	1.46	0.94
Case 7	40,80	1.32	0.71

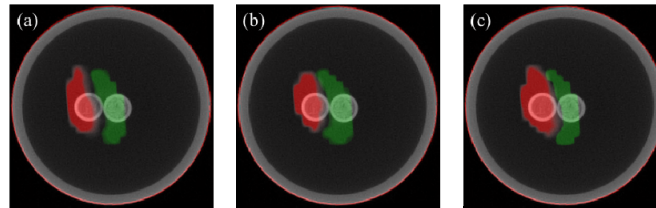


Fig. 7. Tomographic ($z = 1.1$ cm) results of PC2-XLCT obtained from combinations listed in Table 5. Images (a)-(c) correspond to case 1-3, respectively.

3.3 The influence of concentration difference of nanophosphors on target differentiation

Figure 8 shows the results of the proposed method with concentration pairs. In the experiment, four concentration pairs were used and for each concentration pair, X-ray tube voltages of 40 and 50 kV were used to get XLCT images. The first and second rows of Fig. 8 illustrate single-voltage XLCT images of four concentration pairs ($z = 1.1$ cm), indicating that two luminescent targets are difficult to be distinguished when only using measurements acquired at a single X-ray tube voltage. The third to fifth rows of Fig. 8 demonstrate the negative PC2-XLCT, positive PC2-XLCT and fusion images of all concentration pairs, respectively. As shown in Fig. 8, the two tubes containing the same concentration of 50 mg/ml cannot be resolved, due to the light yields of two tubes following same variation trends. All other three pairs can be effectively separated when PCA was applied on two XLCT images acquired at tube voltages of 40 and 50 kV, respectively. The DOCs of three pairs are listed in Table 6. It indicates that with the increase of concentration difference, the average DOC also increases. For the pair of 50-200 mg/ml. the DOC of tube 1 is relatively high. This may be due to the influence of high scattering caused by high concentration of nanophosphors in tube 2 on the distribution of tube 1, considering that they were placed so closely.

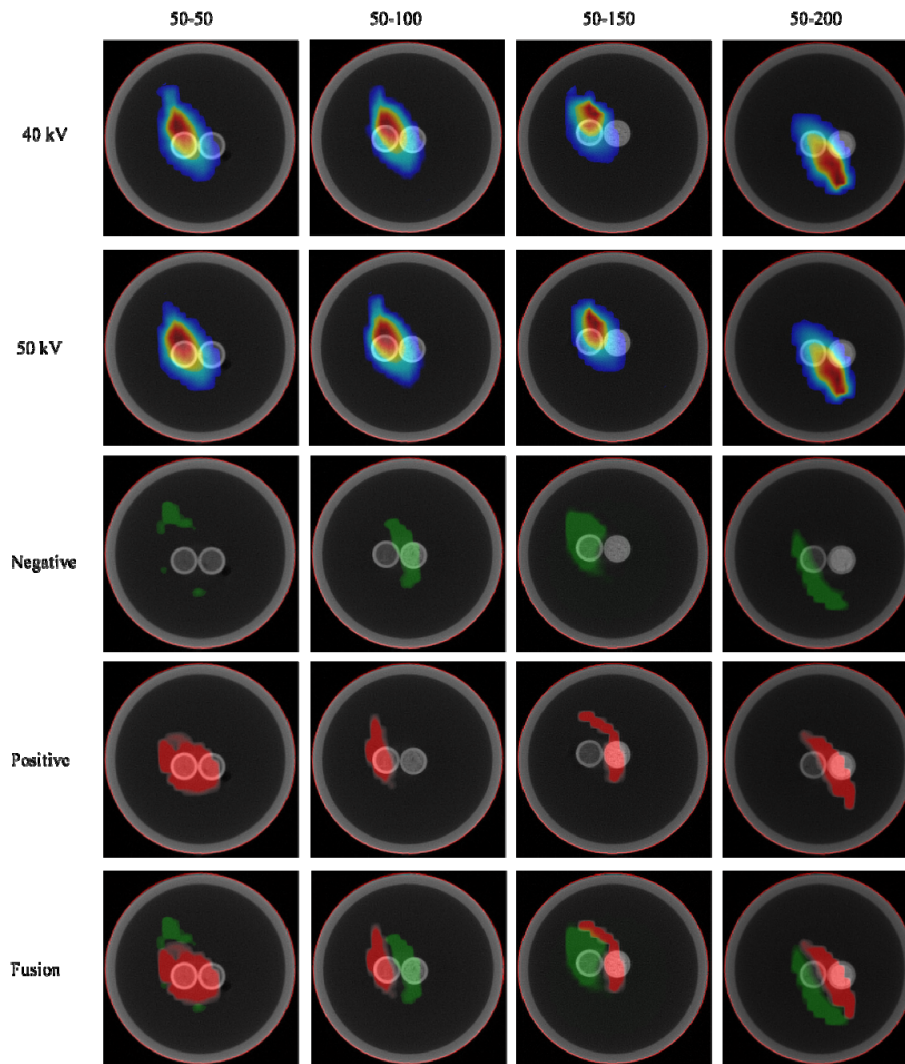


Fig. 8. Tomographic ($z = 1.1$ cm) results of the third experiment. The first two rows show the tomographic reconstruction results corresponding to each excitation X-ray tube voltage obtained by the ART algorithm. The last three rows show the PCs of each case obtained by PCA. The green parts indicate the negative PC2 and the red parts indicate the positive PC2.

Table 6. DOCs of the proposed method with concentration pairs

Concentration pairs	DOC	
	Tube 1 (mm)	Tube 2 (mm)
50-100	1.79	1.22
50-150	1.72	1.94
50-200	2.98	1.18

3.4 Comparison between the fan-beam and cone-beam modes

Figure 9 shows the results of performance of the proposed method in fan-beam mode and cone-beam mode. Images in the first row were reconstructed from cone-beam imaging, while images in the second row were from fan-beam imaging. These results demonstrate that the quality of reconstructed images in the fan-beam mode outperformed that of the cone-beam

mode. However, without the proposed PCA analysis, two adjacent targets could not be resolved even in the fan-beam mode. With the application of PCA on the images reconstructed from the two-voltage excitation, adjacent tubes could be effectively resolved in both modes, though the average DOC (shown in Table 7) of the two tubes in the fan-beam mode was better than that of the cone-beam mode. Considering that fast imaging is desired to monitor nanoparticle-labeled metabolism and drug delivery, the cone-beam mode may be more suitable for *in vivo* XLCT imaging than the fan-beam mode, which obtains better imaging at the cost of time-consuming slice-by-slice scanning.

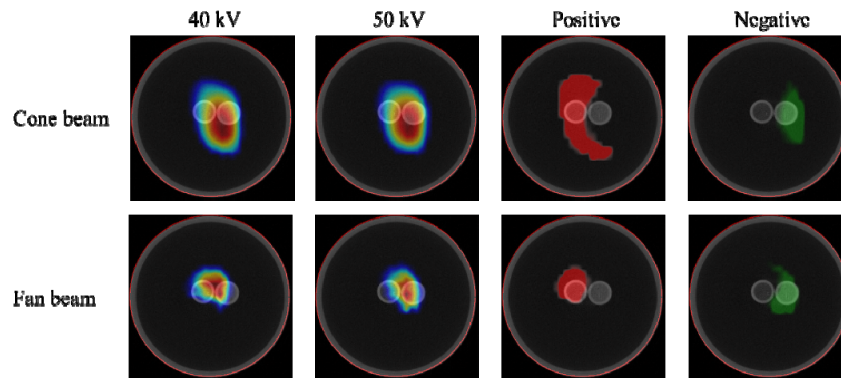


Fig. 9. Tomographic ($z = 1.1$ cm) XLCT and PC2-XLCT results. Images in the first row were reconstructed from cone-beam imaging, while images in the second row were from fan-beam imaging.

Table 7. DOCs of the proposed method for cone-beam and fan-beam imaging mode

Imaging geometry	DOC (mm)	
	Tube 1	Tube 2
Cone-beam	1.10	1.76
Fan-beam	1.40	0.72

4. Discussion and conclusion

As a new dual-mode tomographic imaging modality, cone-beam X-ray luminescence computed tomography has the advantages of high sensitivity and high imaging efficiency, indicating its potential applications in fundamental preclinical experiments. However, due to the nature of highly scattering and weakly absorbing of biological tissues, currently it is quite difficult to resolve adjacent organs with different kinetics (i.e., accumulating concentrations) in small animals. The results of the first phantom experiment in this study revealed that for nanophosphors of different concentrations, the changing rates of photon counts varies with the tube voltage. It indicates that the light output of a nanophosphor behaves differently when excited by X-ray of different tube voltages. Based on the above observation and the multivariate analysis theory, we further propose a PC-based decomposition method on the multi-voltage excitation imaging scheme to resolve two adjacent targets of different nanophosphor concentrations.

The tomographic XLCT images reconstructed from measurements acquired at a given X-ray tube voltage shows that the two tubes with an edge-to-edge distance of 0 cm cannot be separated (Figs. 5 and 8). When PCA is applied to the tomographic XLCT frames, a set of PC images which are linear combination of the frames can be generated. Functional structures with different kinetic patterns can be illustrated in the negative and the positive PC2-XLCT images. In order to test the performance of the proposed method, two phantom experiments were performed to investigate the influence of different excitation combinations and the influence of concentration contrast. The phantom results suggest that the distributions of nanophosphors with different concentrations can be reflected by the positive and negative

PC2-XLCT images with at least two tomographic XLCT frames (Figs. 6 and 7), and the location errors are all less than 2 mm. In addition, the location errors would decrease as the difference of the tube voltage of two frames increase. That's because with larger voltage difference, the difference between light outputs of nanoparticles of different concentrations increased, making the PCA decomposition on reconstructed images more efficient. These findings further confirm that the behavior of nanophosphors of different concentrations relates to the X-ray spectra. Considering that the maximum voltage of the X-ray tube used in this study is 80 kV, the performance of the proposed scheme for tube voltage higher than 80 kV needs further validation. The concentration pair experiment demonstrated that the two tubes cannot be resolved when the concentrations were the same. The location error in the 50-200 mg/ml case is comparatively higher, which may due to the high concentration contrast.

In this study, all the PC-XLCT images are obtained based on the ART results at given X-ray tube voltages, which means the accuracy of the PCs may be affected by the reconstruction ART results. Considering that the performance of PCA could be influenced by many factors including the noise level, reconstruction errors, and the difference between light emitted at different tube voltages, if the noise and reconstruction errors can be reduced by integrating smoothing constrains in the ART framework or by using algorithms based on l_1 -norm [33], better performance could be expected. However, it is still challenging to get relative concentrations of adjacent nanophosphors. To achieve that, optical properties for phosphors of different concentrations, especially their light outputs emitted at different tube voltages, should be known. However, these characteristics seem difficult to obtain, especially in the *in vivo* situation. Other multivariate analysis method, such as independent component analysis [30, 32], can be considered and used in our work.

Clearly with the multi-voltage excitation, the proposed method would increase the imaging time and thus the radiation dose for XLCT imaging. The more the number of tube voltages used, the higher the radiation dose increased. Fortunately, experimental results described above indicate that two adjacent targets could be effectively resolved when a two-voltage excitation was used. Radiation dose measured by an ion chamber (Unfors RaySafe, Sweden) indicated that compared to single tube voltage (40 kV) excited XLCT imaging, the dose increase (27 mGy at 50 kV) was limited, making the proposed scheme still suitable for *in vivo* imaging. In addition, the scanning time and radiation dose of the proposed method could be reduced by using less projections and reconstruction techniques for sparse-view imaging such as compressed sensing-based methods. With a synchronous CT/optical imaging system, the radiation dose could be further decreased. It is also worth noting that the nanophosphors used in this paper is not suitable for *in vivo* experiments, and the *in vivo* experiments should be considered using suitable nanophosphors, such as $\text{NaGdF}_4:\text{Eu}^{3+}$ [34].

In conclusion, the ability of the PCA-based method in resolving structures containing nanophosphors with different concentrations was demonstrated in phantom experiments. In *in vivo* studies, each organ may accumulate different concentrations of nanophosphors and so the light yield of each organ would show different variation trends with X-ray tube voltages. By taking the proposed method, the structures of adjacent organs will be resolved. The proposed can be used in *in vivo* research, such as dynamic studies. Future work will focus on applying the proposed excitation based method to resolve structures of organs in small animals *in vivo*.

Funding

National Key Research and Development Program of China (2017YFC0107400); Natural National Science Foundation of China (NSFC) (81230035); Natural Science Foundation of Shaanxi Province (2016JQ1012); Key project supported by Military Science and Technology Foundation (BWS14C030). Key Science and Technology Program in Social Development of Shaanxi Province (2016SF-044).

Acknowledgments

The authors are grateful to Yuxia Wu and Kaizhong Zheng from the Department of Biomedical Engineering, Fourth Military Medical University, for their kind collaboration.

Disclosures

The authors declare that there are no conflicts of interest related to this article.